Tailoring nanostructured NbCoSn-based thermoelectric materials via crystallization of an amorphous precursor

Jung, Chanwon; Dutta, Biswanath; Dey, Poulumi; Jeon, Seong jae; Han, Seungwoo; Lee, Hyun Mo; Park, Jin Seong; Yi, Seong Hoon; Choi, Pyuck Pa

DOI
10.1016/j.nanoen.2020.105518

Publication date
2021

Document Version
Final published version

Published in
Nano Energy

Nano Energy 80 (2021) 105518

Contents lists available at ScienceDirect

Nano Energy

journal homepage: http://www.elsevier.com/locate/nanoen

Full paper

Tailoring nanostructured NbCoSn-based thermoelectric materials via crystallization of an amorphous precursor

Chanwon Jung [a], Biswanath Dutta [b], Poulumi Dey [b], Seong-jae Jeon [c], Seungwoo Han [c], Hyun-Mo Lee [d], Jin-Seong Park [d], Seong-Hoon Yi [e,*], Pyuck-Pa Choi [a,*]

[a] Department of Materials Science and Engineering, Korea Advanced Institute of Science and Technology (KAIST), 291 Daehak-ro, Yuseong-gu, Daejeon 34141, Republic of Korea
[b] Department of Materials Science and Engineering, Delft University of Technology, Mekelweg 2, 2628 CD Delft, The Netherlands
[c] Department of Nano Mechanics, Korea Institute of Machinery & Materials (KIMM), 156 Gajeongbuk-ro, Yuseong-gu, Daejeon 34103, Republic of Korea
[d] Division of Material Science and Engineering, Hanyang University, 222 Wangsimni-ro, Seongdong-gu, Seoul 04763, Republic of Korea
[e] Department of Materials Science and Metallurgical Engineering, Kyungpook National University, 80 Daehakro, Bukgu, Daegu 41566, Republic of Korea

ARTICLE INFO

Keywords:
Half–Heusler compound
Thermoelectric
Nanocrystallization
Atom probe tomography
Density functional theory

ABSTRACT

Tailoring nanostructures is nowadays a common approach for enhancing the performance of thermoelectric Heusler compounds by decreasing the thermal conductivity without significantly affecting the electrical conductivity. However, the most widely reported method for obtaining nanostructured thermoelectrics, an approach based on crushing as-cast alloy ingots followed by sintering of the debris, only gives limited control of the final nanostructure due to residual elemental segregation after casting. Here, a novel approach for fabricating nanostructured Heusler compounds is presented, which is based on crystallizing an amorphous precursor of $NbCo_{1.1}Sn$ composition. This method yields two distinct nanostructures, namely one comprising only half-Heusler grains and another one comprising half-Heusler grains and full-Heusler nano-precipitates. The latter sample exhibits enhanced negative Seebeck coefficients as compared to the former over a wide temperature range. Using advanced characterization techniques, such as high-resolution transmission electron microscopy and atom probe tomography, in conjunction with ab initio density functional theory, detailed insights into the nanostructure and electrical properties of the specimens are provided. Filtering of low energy and mobility electrons at the half-Heusler and full-Heusler interface along with the formation of Co interstitial defects in the half-Heusler matrix are proposed to be the possible causes for the enhanced Seebeck coefficient of the nano-precipitate containing specimen.

1. Introduction

Among various technologies for sustainable energy production thermoelectric devices are particularly attractive as they enable conversion of waste heat into valuable electrical energy [1–7]. A recent report states that 68% of the energy produced in 2018 in the U. S. was lost mainly in the form of waste heat [8], clearly indicating that there is huge potential for making use of large-scale thermoelectric power generation [9]. However, practical usage of thermoelectric devices has been limited by their low energy conversion efficiencies.

The performance of thermoelectric materials is assessed by the figure of merit, $zT = \alpha^2\sigma T(\kappa_L+\kappa_e)^{-1}$, where α is the Seebeck coefficient, σ is the electrical conductivity, T is the absolute temperature, and κ_L and κ_e are the lattice thermal conductivity and electronic thermal conductivity, respectively. In order to achieve a high figure of merit, the power factor ($\alpha^2\sigma$) should be enhanced while decreasing the thermal conductivity ($\kappa_L+\kappa_e$). However, the physical properties, α, σ, and κ_e, are coupled to each other, as they all depend on the charge carrier concentration. Thus, independent control of these physical properties has remained a central challenge for accomplishing a high zT value.

For the intermediate temperature range between 773 and 1073 K, for which abundant industrial waste heat sources are available, lead chalcogenides [10,11], skutterudites [12,13], and half-Heusler compounds [14–16] have been intensively studied. Among them, half-Heusler compounds are advantageous in terms of their high thermal stability [17], mechanical robustness [18], high Seebeck coefficients [19,20],

* Corresponding authors.
E-mail addresses: yish@knu.ac.kr (S.-H. Yi), p.choi@kaist.ac.kr (P.-P. Choi).

https://doi.org/10.1016/j.nanoen.2020.105518
Received 3 August 2020; Received in revised form 12 October 2020; Accepted 18 October 2020
Available online 20 October 2020

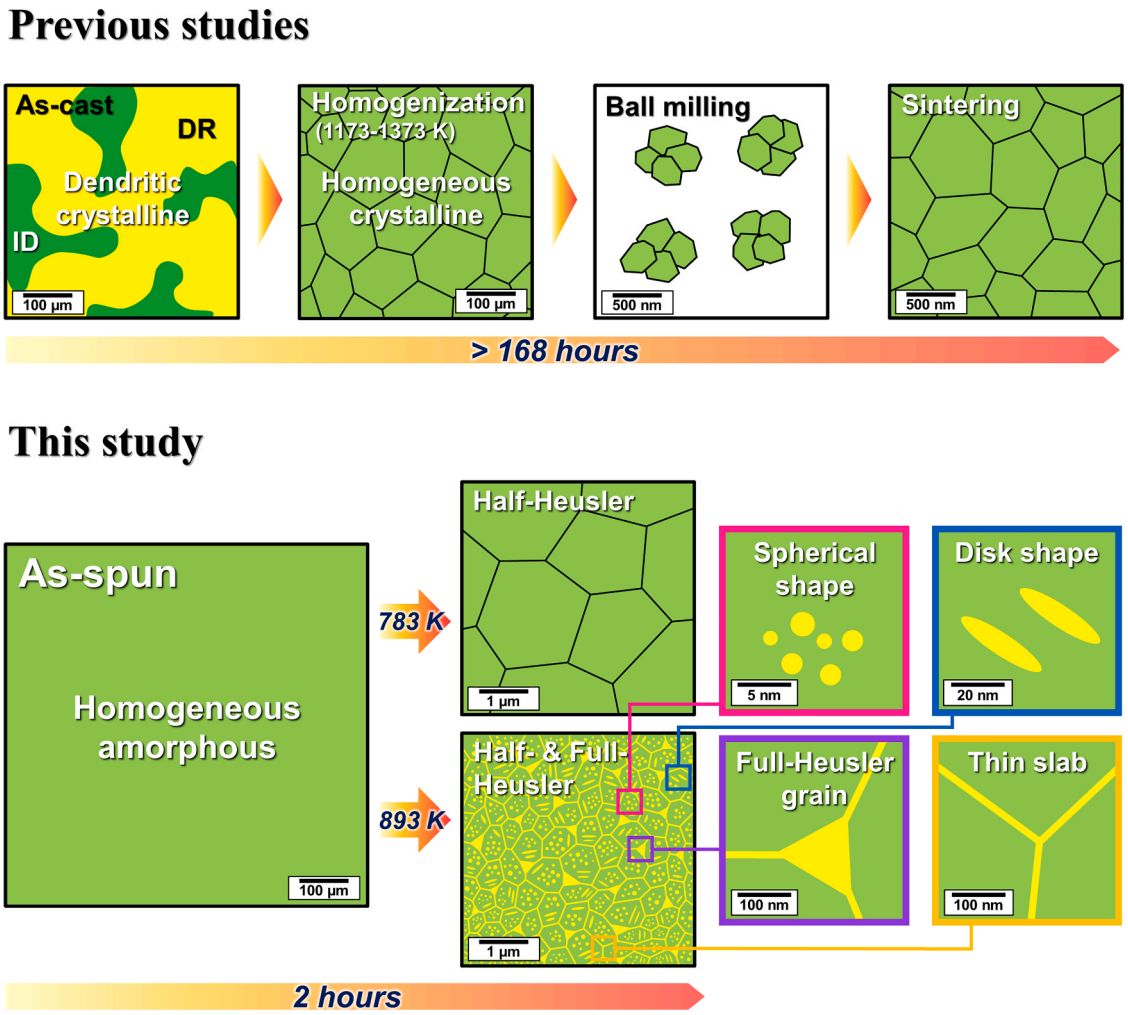

Fig. 1. Schematic illustrations of the methods for forming nanostructured Heusler compounds. Top: conventional approach using ball milling and sintering. Bottom: novel approach proposed in this study, based on crystallization of an amorphous precursor.

high power factor [21], non-toxicity [22], and usage of earth-abundant elements [23]. However, these beneficial properties are compromised by a relatively large lattice thermal conductivity, limiting the figure of merit [24,25].

In order to overcome this drawback, fabrication of nanostructured thermoelectric materials, e. g., through grain refinement or nano-precipitation has been recently explored with some promising results. For instance, nanocrystalline FeVSb-based half-Heusler compounds were reported to exhibit lower lattice thermal conductivity than their polycrystalline counterparts [26]. This phenomenon was related to the mean free path (MFP) of phonons, which amounted up to 300 nm at ~ 650 K, a distance comparable to the average grain size of the reported polycrystalline half-Heusler compounds. In contrast, the MFP of charge carriers was found to be only a few nm [27] and hence, grain boundaries in nanocrystalline half-Heusler compounds could efficiently reduce the thermal conductivity without significantly affecting the electrical conductivity [28]. Moreover, simultaneous enhancements in Seebeck coefficient and electrical conductivity were observed for materials containing full-Heusler nano-precipitates [29,30]. The above-mentioned studies have shown that formation of nanostructures through grain- and phase boundaries is a promising approach for controlling transport of electrons and phonons and hence the thermoelectric properties.

The most widely reported method for fabrication of nanostructured half-Heusler compounds is an approach based on crushing cast coarse-grained alloy ingots by means of ball milling for grain refinement followed by sintering of the resulting powder (see Fig. 1) [31–33]. A major disadvantage of this approach is that precise control of the final nanostructure is not possible due to residual elemental segregation after casting. In order to remove micro- or macro-segregation of as-cast ingots, high energy ball milling can be applied. However, under certain circumstances extensive heat treatments of the cast ingots at 1173–1373 K for typically more than 168 h are required due to the low diffusivities of the heavy group four and five elements, Zr, Hf, Nb, and Ta [34,35]. Thus, thermal processing of as-cast ingots containing these elements is time and energy consuming and impracticable for large-scale fabrication of Heusler compounds.

Here, we propose a novel approach for fabricating nanostructured Heusler compounds with promising thermoelectric properties, which is based on crystallizing an amorphous precursor (see Fig. 1). The initial amorphous material, which does not show any long-range order, is prepared in the form of ribbons by means of melt-spinning. Due to the extremely high cooling rates associated with this technique, one can obtain well-defined homogenous samples with negligible chemical segregation. No homogenization treatment is required, thus saving a substantial amount of time and energy. Instead, one can directly apply a short low-temperature heat treatment to induce nanocrystallization. Through a careful selection of the crystallization temperature and time one can obtain a nanostructure, which comprises a half-Heusler matrix and full-Heusler nano-precipitates and shows beneficial thermoelectric

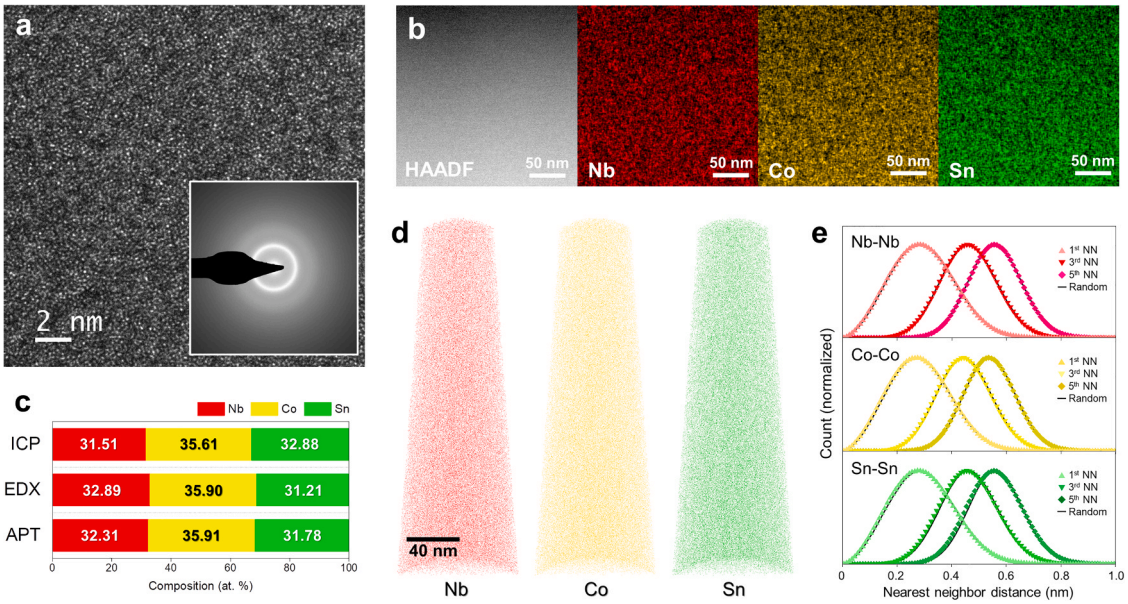

Fig. 2. (a) HR-TEM image, (b) EDX elemental maps of as-spun amorphous $NbCo_{1.1}Sn$. (c) chemical compositions of as-spun amorphous $NbCo_{1.1}Sn$ acquired from various methods. (d) APT reconstruction of as-spun amorphous $NbCo_{1.1}Sn$ and (e) 1st, 3rd and 5th nearest neighbor distribution for each alloying element.

properties.

In order to demonstrate the viability of such a process, we chose an alloy of $NbCo_{1.1}Sn$ composition. The role of the excess Co was to induce formation of $NbCo_2Sn$ full-Heusler precipitates in a NbCoSn half-Heusler matrix through a heat treatment (see Fig. 1). The annealing conditions for the specimens studied herein were selected based on differential scanning calorimetry (DSC) measurements (see Supplementary data for details). While the first specimen was annealed at a relatively low temperature, *i. e.* at 783 K, and exhibited only half-Heusler grains formed by crystallization of the amorphous precursor, the second specimen was annealed at a higher temperature, *i. e.* 893 K, and comprised half-Heusler grains and full-Heusler nano-precipitates.

We used advanced characterization techniques such as Cs-corrected transmission electron microscopy (TEM) and atom probe tomography (APT) to characterize the crystal structures and reveal the elemental partitioning at the sub-nanometer scale. In addition, we performed comparative measurements of Seebeck coefficients as a function of temperature. In order to understand the measured differences in Seebeck coefficient, an electronic energy band diagram including the work functions of each phase was deduced from experiments and ab initio density functional theory (DFT) calculations.

We note that the present paper focuses on the relationship between the observed nanostructures and the measured physical properties. A discussion on the nanocrystallization process of the amorphous precursor, based on thermodynamic and kinetic considerations, will be given elsewhere.

2. Results and discussion

2.1. Nano-characterization of specimens before and after heat treatments

Fig. 2a shows a high-resolution TEM (HR-TEM) image of an as-spun sample. No lattice fringes could be observed, and moreover, only halo rings typical of an amorphous structure (see inset of Fig. 2a) could be seen in a selected area electron diffraction (SAED) pattern. The amorphous structure of the as-spun sample could also be confirmed by means of X-ray diffraction (XRD), where the XRD pattern only exhibited a pronounced halo peak (see Fig. S2a). Although the presence of a very small fraction of a crystalline phase could not be completely excluded due to limitations in the field-of-view of TEM and detection sensitivity of XRD, it is safe to conclude that the as-spun alloy was predominantly amorphous. In the next step, we investigated the thermal stability of the amorphous structure by performing XRD analyses on specimens annealed up to 563, 673, and 783 K in the DSC instrument. All specimens exhibited a broad halo peak, where only the specimen annealed at 783 K exhibited an additional peak that could be identified as the (220) reflection of the crystalline half-Heusler NbCoSn compound (see Fig. S2b). We note that only a single exothermic peak was detected in the DSC measurement (see Fig. S1a), where the onset and peak temperature amounted to 757 K and 833 K, respectively. As the final heating temperature (783 K) of the partially crystallized specimen (see Fig. S2b) was within the range between onset (757 K) and peak temperature (833 K), the detected DSC peak could be unambiguously ascribed to the crystallization of the amorphous precursor. We did not detect any pronounced glass transition by means of DSC, presumably due to a small difference between glass transition and crystallization temperature for the alloy studied herein.

Energy dispersive X-ray spectroscopy (EDX) maps revealed homogeneous distributions of the alloying elements (see Fig. 2b), where the chemical composition of the mapped area was 32.9 ± 2.1 at% Nb, 35.9 ± 1.5 at% Co, and 31.2 ± 8.4 at% Sn. These values were in good agreement with inductively coupled plasma-optical emission spectrometry (ICP-OES) and APT results (compare Fig. 2c). Furthermore, we confirmed the homogeneity of the elemental distributions through APT reconstructions (see Fig. 2d) and corresponding nearest neighbor distribution analyses (see Fig. 2e).

In order to induce crystallization of the amorphous precursor into nanostructured Heusler compounds, we performed isothermal annealing at 783 and 893 K for 2 h. In the following, we denote the $NbCo_{1.1}Sn$ specimens annealed at 783 and 893 K as NCS-783 and NCS-893, respectively. For both temperatures, we detected the NbCoSn half-Heusler compound as the main constituent phase (see Fig. S3), whereas the $NbCo_2Sn$ full-Heusler phase was only observed after annealing at 893 K. Fig. 3a and 3b shows scanning transmission electron microscopy-high angle annular dark field (STEM-HAADF) images of the NCS-783 and NCS-893 specimen, respectively. In both specimens we observed columnar half-Heusler grains near the surface, while the bulk regions were composed of equiaxed grains. The NCS-893 specimen showed much finer grains than the NCS-783 specimen. This difference in grain size can be explained by considering the kinetics of crystallization

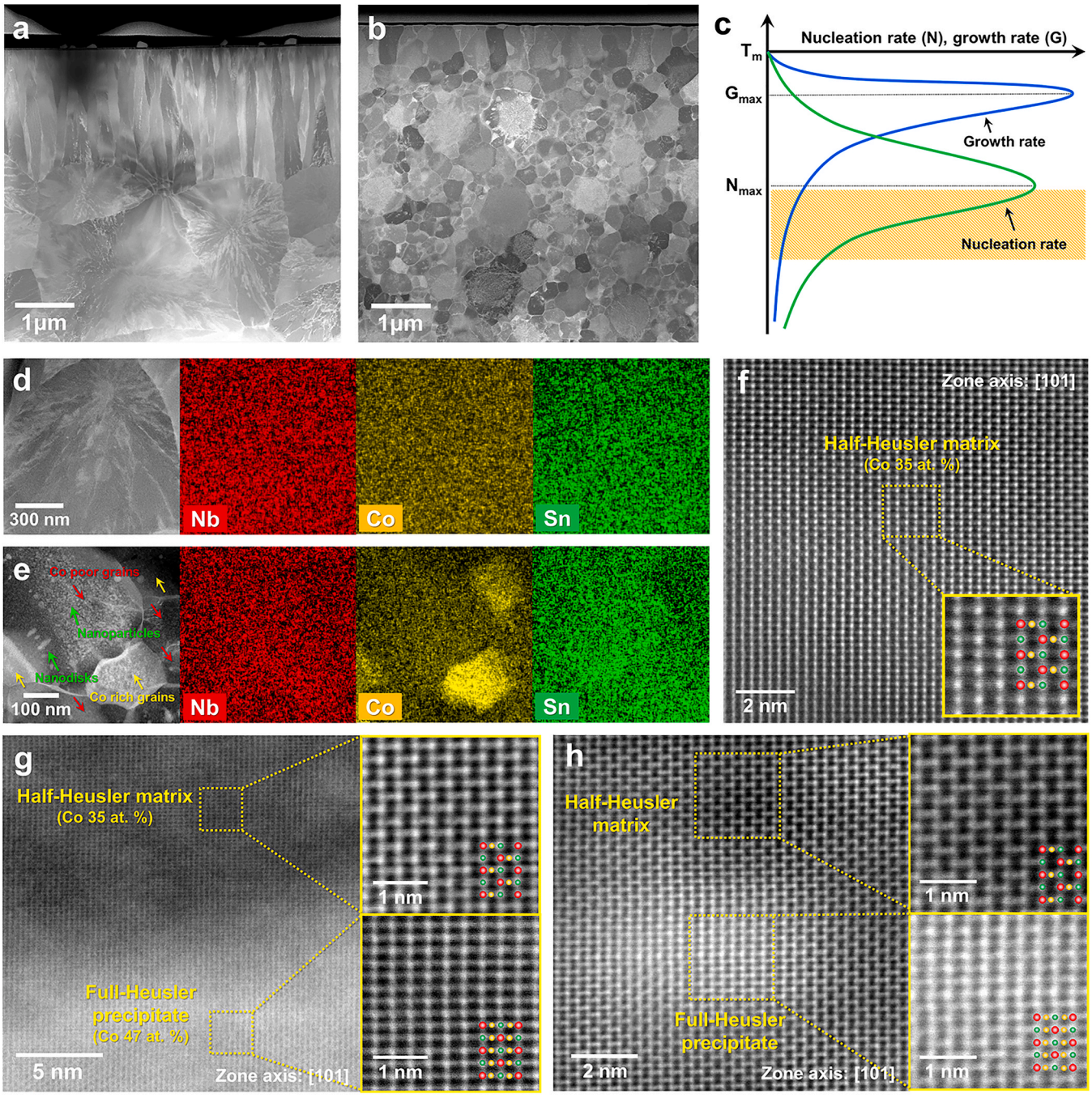

Fig. 3. STEM-HAADF images of the (a) NCS-783 and (b) NCS-893 specimen and (c) schematic diagram of nucleation rate and growth rate as a function of temperature. EDX maps of the (d) NCS-783 and (e) NCS-893 specimen. High-resolution STEM-HAADF images of the (f) half-Heusler matrix of the NCS-783 specimen, (g) phase boundary between half-Heusler and full-Heusler phases and (h) full-Heusler nano-precipitate in a half-Heusler matrix in the NCS-893 specimen.

of metallic glasses [36]. The temperature region in which crystallization of a metallic glass takes place is significantly lower than the melting temperature (the yellow region in Fig. 3c). The nucleation rate substantially increases with increasing temperature in this region, while the growth rate of nucleated nanocrystals increases much more slowly. As a result, crystallization at 893 K yields a finer grain structure than crystallization at 783 K. In addition, we did not observe any remarkable grain growth after long-term heat treatment of 12 h (see Fig. S4), suggesting that the grain growth kinetics at these two temperatures are sluggish and that the difference in grain sizes between the NCS-783 and NCS-893 specimens can be explained in terms of the nucleation kinetics rather than the growth kinetics.

Fig. 3d and e shows STEM-EDX results for the NCS-783 and NCS-893 specimen, respectively. While the former exhibited a single-phase microstructure with homogeneous distributions of the alloying elements (Fig. 3d), the latter showed Co rich grains in the matrix (Fig. 3e) with an average chemical composition of 27.8 ± 2.3 at% Nb, 46.6 ± 2.0 at% Co, and 25.6 ± 7.5 at% Sn, close to the expected stoichiometric composition of the full-Heusler phase. The volume fraction and average grain diameter of the Co rich grains was about 6.2% and 152 ± 36 nm, respectively (Fig. S5). For the residual matrix an average chemical composition of 33.1 at. ± 2.5% Nb, 35.6 ± 1.5 at% Co, and 31.3 ± 8.8 at% Sn was measured, which was close to the stoichiometric composition of the NbCoSn half-Heusler phase. In the grain interior

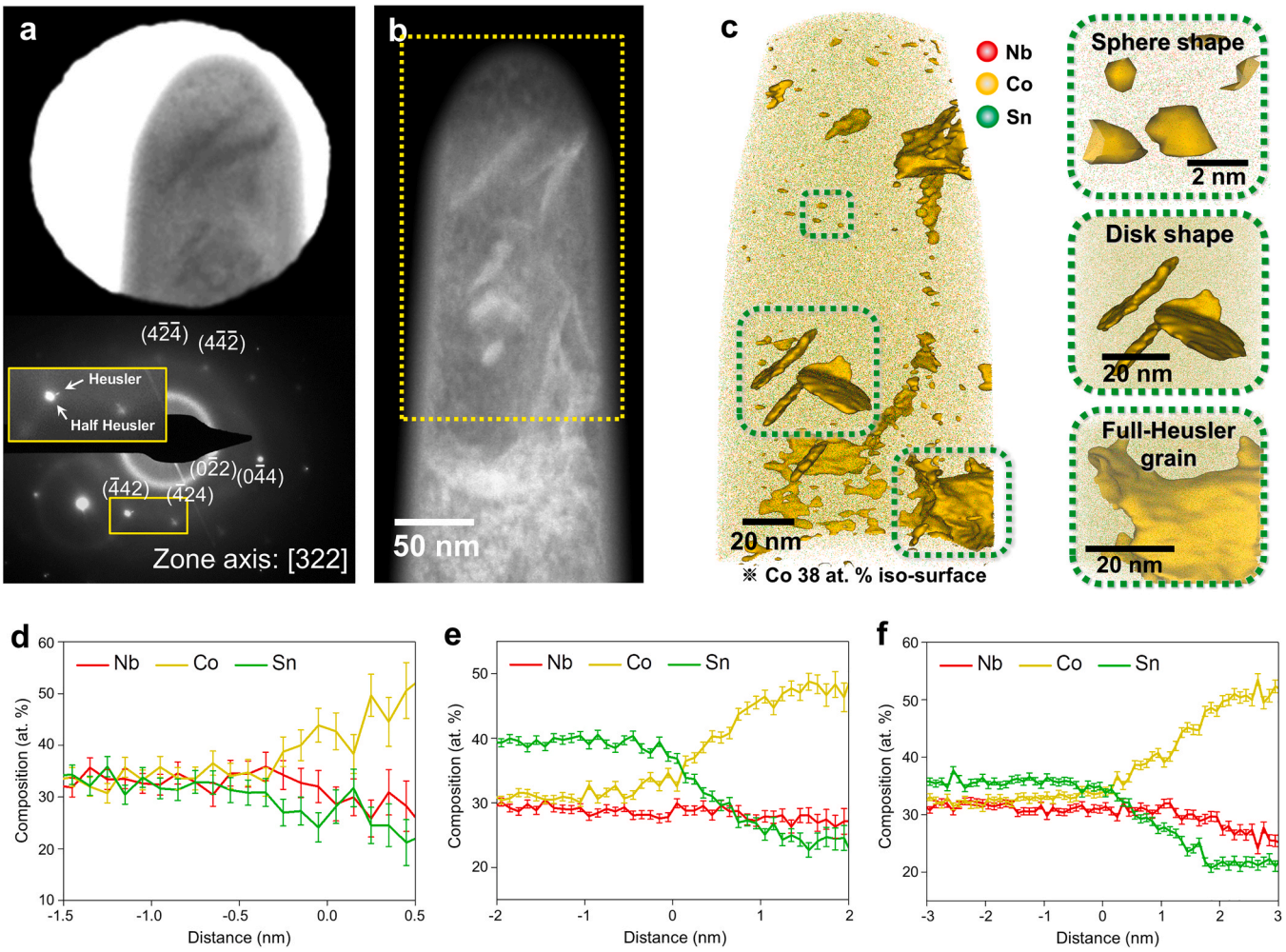

Fig. 4. (a) TEM image of an APT tip with aperture (SAED pattern included as an inset). (b) STEM-HAADF image, and (c) 3d atom maps of NCS-893, including iso-concentration surfaces of 38 at% Co (insets show enlarged views of the regions marked by dashed rectangular boxes), and the proxigrams based on iso-concentration surfaces of 38 at% Co for (d) spherical nano-precipitates, (e) disk-shaped nano-precipitates, and (f) full-Heusler grain.

regions, we observed two types of nano-precipitates of spherical and disk shape. The majority of nano-precipitates exhibited a near-spherical shape with a diameter of 2.3 ± 1.3 nm. The number density of the spherical precipitates was 4.3×10^{-3} nm^{-2}. Disk-shaped precipitates of a diameter of 38 ± 13 nm and a thickness of 13 ± 2 nm were observed, in the region near grain boundary (Fig. 3e). The number density of the disk-shaped precipitates was 5.6×10^{-5} nm^{-2}, which is significantly lower than that of spherical precipitates. These nano-precipitates were present in all Co poor grains, but not in Co rich grains.

Fig. 3 includes high-resolution STEM-HAADF images of a grain interior region of the NCS-783 sample (Fig. 3f) and of precipitates and the matrix of the NCS-893 sample (Fig. 3g and 3h). The NCS-783 specimen exhibited lattice fringes and a sub-lattice occupancy along the [101] zone axis, which exclusively matched the half-Heusler phase (see Fig. 3f). The full-Heusler phase was not detected in this specimen. In contrast, the NCS-893 specimen contained both the Co poor half-Heusler phase and the Co rich full-Heusler phase, which could be clearly distinguished from each other by the mass contrast of the STEM-HAADF images and their different sub-lattice occupancy (see insets in Fig. 3g). Using high-resolution TEM, we measured a lattice constant value of 0.608 nm for the half-Heusler phase in the NCS-783 specimen (see Fig. S6a). In comparison, the lattice parameter of half-Heusler matrix of the NCS-783 specimen was 0.596 nm (see Fig. S6b) and thus reduced, as excess Co in the $NbCo_{1.1}Sn$ half-Heusler matrix partitioned to the $NbCo_2Sn$ full Heusler precipitates. This finding is consistent with previous studies on $ZrNi_{1+x}Sn$-based Heusler compounds [37,38]. Besides full-Heusler grains of an average diameter of 152 ± 36 nm, we observed fine nanometer-sized full-Heusler precipitates inside the half-Heusler grains (see Fig. 3h). Due to the structural similarity between the half- and full-Heusler phases and similar lattice parameters, the phase boundaries were coherent.

The NCS-893 sample was closely examined by means of correlative TEM-APT characterization. Fig. 4a shows a selected area TEM image of an APT specimen and the corresponding SAED pattern, with which we could confirm the co-existence of coherent half- and full-Heusler phase. The latter showed a bright contrast in STEM-HAADF images (see Fig. 4b). Fig. 4c shows an APT reconstruction acquired from the same specimen, including iso-concentration surfaces with a threshold value of 38 at% Co. A complex nanostructure comprising spherical and disk-shaped full-Heusler nano-precipitates inside half-Heusler grains and a coarse full-Heusler grain (bottom region of APT map) was detected, which were all enriched with Co (> 38 at%). The average diameter and number density of the spherical nano-precipitates were 2.3 ± 1.0 nm and 1.3×10^{-3} nm^{-3}, respectively, while disk-shaped nano-precipitates showed an average diameter of 33.5 ± 8.3 nm, a thickness of 4.9 ± 0.9 nm and a number density of 7.5×10^{-6} nm^{-3}. We could identify these Co rich regions as the full-Heusler phase through direct correlations with STEM images. Fig. 4d-f show proximity histograms (proxigrams) across spherical shaped as well as disk-shaped nano-precipitates and a full-Heusler grain, respectively. All proxigrams

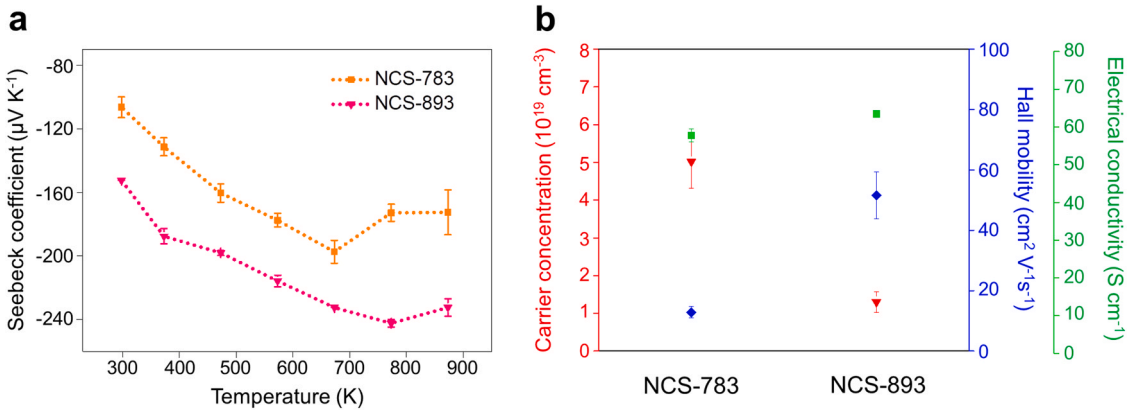

Fig. 5. (a) Seebeck coefficients of the NCS-783 and NCS-893 as a function of temperature and (b) Hall measurement results for annealed $NbCo_{1.1}Sn$ ribbons at 710 K.

were determined with respect to interfaces defined by iso-concentration surfaces of 38 at% Co. The Co concentrations in the regions of interest increased to near 50 at% towards their cores, i.e. close to the stoichiometric composition of the full-Heusler phase ($NbCo_2Sn$), whilst Sn was depleted. In addition to the precipitates in the grain interior, we detected thin slabs of full-Heusler precipitates decorating the grain boundaries of half-Heusler grains (see Fig. S7a-d). Unlike the NCS-893 specimen, for which various precipitates were observed, the APT reconstructions acquired from the NCS-783 specimen revealed homogeneous elemental distributions (see Fig. S8). The average chemical composition of the analyzed volume in Fig. S8 was 31.9 ± 0.1 at% Nb, 34.5 ± 0.1 at% Co, and 33.4 ± 0.1 at% Sn, showing an excess Co concentration. In conjunction with XRD results (Fig. S2a and S3), we may conclude that a polymorphic transformation from an amorphous to a half-Heusler structure occurred for this specimen (NCS-783).

2.2. Measurements of thermoelectric properties

Next, we measured the Seebeck coefficients of the heat-treated samples in the temperature range from 300 to 873 K (see Fig. 5a). Both samples (NCS-783 and NCS-893) exhibited negative Seebeck coefficients and thus n-type conductivity. The Seebeck coefficients decreased with increasing temperature and reached a minimum of − 197.4 μV K^{-1} at 673 K and of − 242.3 μV K^{-1} at 773 K for the NCS-783 and NCS-893 specimen, respectively. The latter showed a more negative Seebeck coefficient (by about 45 μV K^{-1}) than the former throughout the entire considered temperature range. In addition, temperature-dependent electrical conductivity measurements revealed a larger electrical conductivity and consequently a larger power factor for the NCS-893 specimen than for the NCS-783 specimen (see Fig. S9).

For further analyses of the electrical properties, we conducted Hall measurements (see Fig. 5b). Both samples exhibited n-type behavior in agreement with the Seebeck coefficient measurements. Furthermore, the NCS-893 sample exhibited a smaller carrier concentration and higher Hall mobility as well as electrical conductivity than the NCS-783 sample in the temperature range from 310 to 710 K (see Fig. 5b and S10). Therefore, the enhancement of the Seebeck coefficient for NCS-893 can be ascribed to a lower carrier concentration than NCS-783.

The measured thermal conductivity values were 2.51 ± 0.19 W/mK, 3.70 ± 0.32 W/mK and 2.75 ± 0.18 W/mK for as-spun $NbCo_{1.1}Sn$, NCS-783 and NCS-893 specimens, respectively. Compared to previously reported room temperature thermal conductivity values of NbCoSn (6.0–9.9 W/mK [39–44], see Table S1), the specimens studied in this work showed lower values (2.51 – 3.70 W/mK). In addition, we divided the contributions to the total thermal conductivity into lattice thermal conductivity and electronic thermal conductivity, as described in [44]. The Wiedemann–Franz law ($\kappa_e = L\rho^{-1}T$) with a Lorentz number of $L = 2.0 \times 10^{-8}$ V^2 K^{-2} for a degenerated semiconductor [26] was used to estimate the carrier contribution to the total thermal conductivity. Among the measured specimens, as-spun $NbCo_{1.1}Sn$ showed the lowest lattice thermal conductivity due to the absence of long-range ordering (see Table S2). Furthermore, the thermal conductivity of NCS-893 was almost twice as low as that of NCS-783 most likely due to the large number of full-Heusler nano-precipitates promoting phonon scattering at phase boundaries.

We obtained room temperature a zT value of 0.006 for the NCS-893 specimen, which was slightly lower than other values of 0.007 [39] and 0.013 [44] reported for NbCoSn at room temperature. However, we anticipate that our specimens will show higher zT values at elevated temperatures than previously reported specimens, as they show a substantially lower thermal conductivity.

2.3. Energy filtering effect by full-Heusler nano-precipitates

To deduce the electronic band alignment between the half-Heusler and full-Heusler compounds, we performed ultraviolet photoelectron spectroscopy (UPS) experiments on both reference bulk half-Heusler (NbCoSn) and full-Heusler ($NbCo_2Sn$) specimens (see Fig. 6a) and estimated the work functions of each phase using following equation:[45].

$$\phi = h\nu - \left|E_F - E_{cutoff}\right|, \quad (1)$$

where ϕ is the work function, $h\nu$ is the incident photon energy (21.2 eV for He I), E_F is the Fermi energy, and E_{cutoff} is the cut-off energy. The Fermi energy of both samples corresponds to a binding energy of 0, where the binding energy increases with electrons coming from a deeper energy level. While the determined cut-off energies of NbCoSn and $NbCo_2Sn$ were 16.52 and 16.38 eV, respectively, the work functions of NbCoSn and $NbCo_2Sn$ were 4.68 eV and 4.82 eV, respectively.

To validate the UPS results, we determined the work functions using DFT by subtracting the Fermi energy from the vacuum potential energy. When calculating the work functions for NbCoSn and $NbCo_2Sn$, we chose the thickness of the vacuum slab to be large enough such that the potential energy in the middle of the vacuum slab was not sensitive to the thickness. A schematic illustration of the slab model is presented in Fig. S11. Fig. 6b and 6c show the electrostatic potential energy along the z axis for NbCoSn and $NbCo_2Sn$. While constant potential energies were confirmed for the center regions of the vacuum slabs, the calculated work functions of NbCoSn and $NbCo_2Sn$ were 3.96 eV and 4.11 eV, respectively. Thus, the difference between the work functions of the half-Heusler and the full-Heusler phases as obtained from DFT calculations (0.15 eV) is in excellent agreement with the UPS measurements (i.e. 0.14 eV).

Fig. 6d shows a schematic band diagram across the NbCoSn and $NbCo_2Sn$ interface, deduced from the UPS measurements and DFT

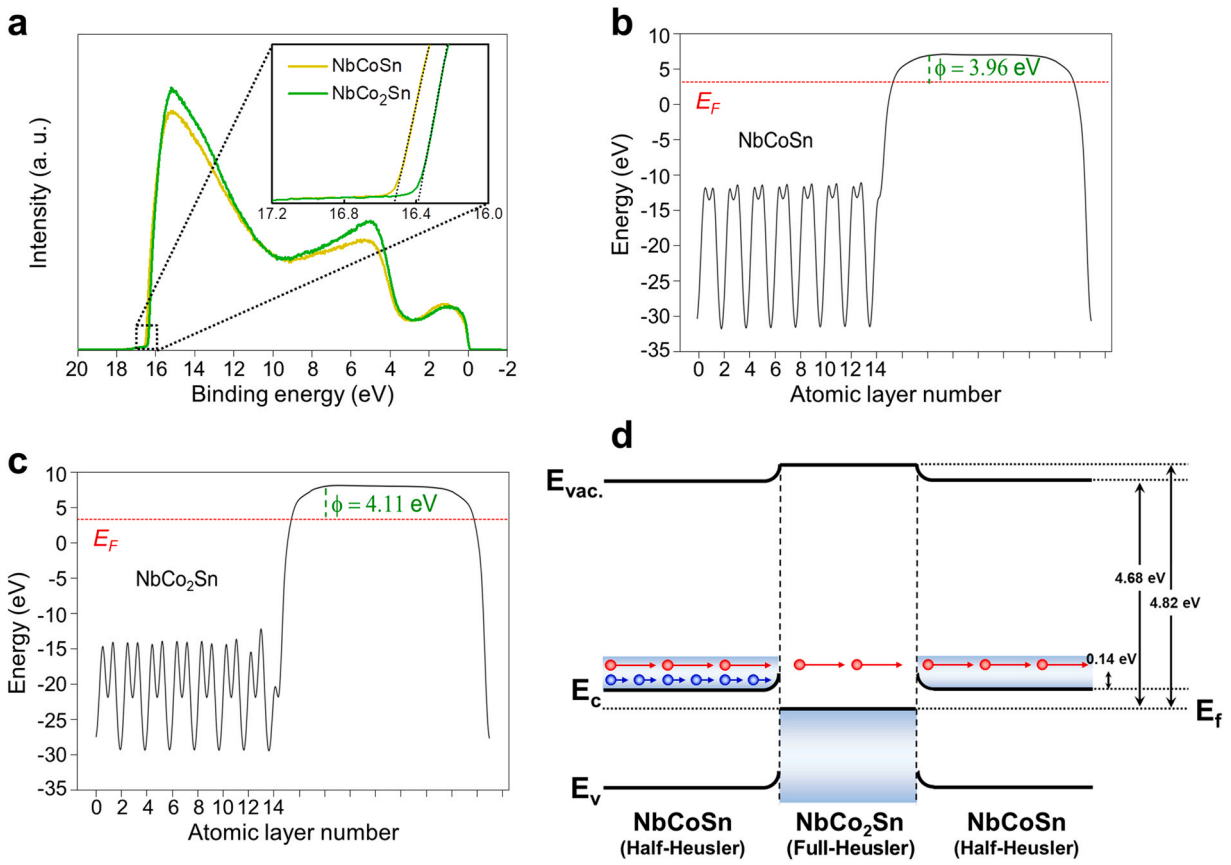

Fig. 6. (a) UPS results and electrostatic potential curve in the *z* direction for (b) NbCoSn and (c) $NbCo_2Sn$ obtained within DFT. The Fermi energy is indicated by E_F. The values of the work functions (ϕ) are indicated in the corresponding sub-figures. (d) Schematic band diagram of the interface between NbCoSn and $NbCo_2Sn$.

calculations. Since full-Heusler and half-Heusler compounds are reported to be half-metals [46] and semiconductors [41], respectively, a Schottky contact is expected to be formed at the phase boundaries between NbCoSn and $NbCo_2Sn$ [47]. The conduction band edge for NbCoSn is expected to be bended upwards owing to its work function difference with $NbCo_2Sn$. As a result, an energy barrier of about 0.14 eV in height should be generated at the conduction band edge for NbCoSn, which is validated by the DFT calculations. In addition, spherical nano-precipitates (NPs) with a radius of a few nano-meters could give rise to an increase in the energy barrier. When a photoelectron is emitted from a phase, a positive charge is left on the remaining surface. For a bulk material, the remaining charge is evenly distributed over a semi-infinite surface. Due to a diminishingly low charge density on the semi-infinite surface the attraction between electrons and the surface is negligible. However, for nano-precipitates, the charge is confined to a small surface. Coulombic attraction with surface charge hinders electrons from escaping, where the resulting work function increase can be quantitatively expressed by the following equation [48].

$$\phi_{NPs} = \phi_{bulk} + \frac{5.4}{R}$$

ϕ_{NPs} and ϕ_{bulk} are the work functions of the nano-precipitates and bulk materials, respectively, and R is the radius of the nano-precipitates in Å. For the spherical full-Heusler nano-precipitates, which were the main population of precipitates observed in the NCS-893 specimen and which showed an average radius of 2.3 nm, the above equation yields an increase in work function and energy barrier of 0.47 eV.

The energy barrier estimated above may act as a filter for low energy electrons of low mobility, also referred to as the energy filtering effect [49–51]. As a result, a reduced carrier concentration for the NCS-893 specimen, comprising both a half-Heusler NbCoSn matrix and full-Heusler $NbCo_2Sn$ nano-precipitates may lead to enhanced Seebeck coefficients (see Fig. 5).

2.4. *Co interstitial defects in the $NbCo_{1.1}Sn$ heat treated at 783 K*

In contrast to the NCS-893 specimen, NCS-783 forms a single-phase half-Heusler matrix of $NbCo_{1.1}Sn$ composition, suggesting the existence of excess Co as point defects. Previous DFT studies on TiNiSn half-Heusler compounds showed that excess Ni atoms, occupying structural interstitial sites (termed as Ni interstitials) are energetically favorable [52,53]. The energy states of the *d* orbitals of Ni were found to exist below the valence band. However, the *d* orbitals of Ni interstitials exhibited poorer bonding with Sn and higher energy than the *d* orbitals between regular Ni and Sn atoms. As a result, Ni interstitials produced energy states in the bandgap [53,54]. In addition, Barczak et al. [55] reported that Ni interstitials reduced the bandgap, which led to an increase in carrier concentration. The latter caused a reduction in both Seebeck coefficient and Hall mobility.

DFT calculations were performed within this work for Co interstitial and antisite defects in order to examine whether the above-described phenomenon for Ni interstitials is valid for the NCS-783 specimen. The energetics probed within DFT calculations revealed that the Co interstitials are energetically more favorable than Co antisite defects since the formation energy of the former was found to be lower than the latter by approximately 2 eV (see Table S3). In order to mimic the NCS-783 specimen (with excess Co) within DFT, two Co interstitials were introduced in the 96-atom supercell of NbCoSn (i.e., $NbCo_{1.06}Sn$) and the corresponding density of states (DOS) was explored (Fig. 7a). The obtained DOS was subsequently compared with the DOS (Fig. 7b) of NbCoSn with one extra Co interstitial (i.e., $NbCo_{1.03}Sn$) in order to

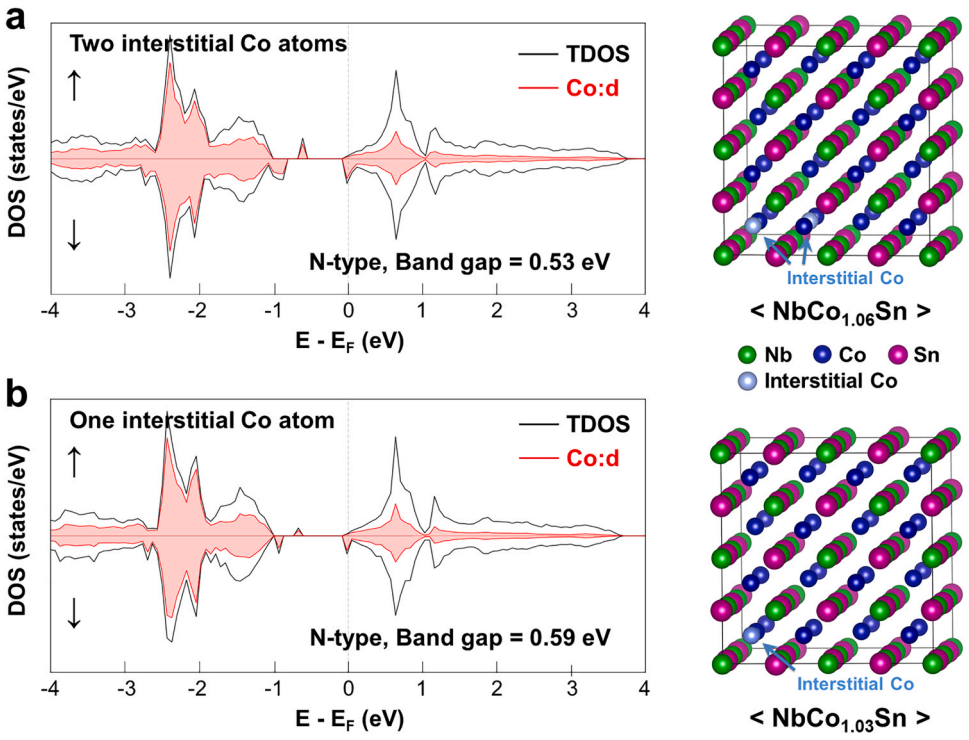

Fig. 7. Density of states calculated using DFT and supercell structure for (a) $NbCo_{1.03}Sn$ and (b) $NbCo_{1.06}Sn$.

underscore the changes induced by extra Co atoms in the DOS of the half-Heusler. The calculations revealed that the interstitial Co defect in NbCoSn is stabilized in a ferromagnetic state. Fig. 7a and b shows that the density of the mid-gap state in the up-spin channel increases with increasing concentration of Co interstitials. Similarly, the peak in the down-spin channel near the Fermi level also increases with the increase in the number of Co interstitials. The calculated band gap for $NbCo_{1.06}Sn$ (0.53 eV) is lower than the band gap for $NbCo_{1.03}Sn$ (0.59 eV). A comparison of the above values with the band gap of 0.97 eV for the defect free NbCoSn (not shown here) clearly indicates that the band gap decreases with increasing amount of Co interstitials. Thus, the formation of mid-gap states leading to a reduced bandgap can be regarded as another cause for an increased carrier concentration and a reduced Seebeck coefficient for NCS-783 as compared to NCS-893.

3. Conclusions

In this study we proposed a novel approach for fabricating nanostructured Heusler compounds with promising thermoelectric properties through nanocrystallization of an amorphous precursor. In order to demonstrate the feasibility of our method, we prepared amorphous melt-spun ribbons of a $NbCo_{1.1}Sn$ alloy, subjected them to crystallization at 783 and 893 K for 2 h and characterized the resulting nanostructures and thermoelectric properties. Using advanced characterization techniques, such as STEM-HAADF and APT, we detected coherent full-Heusler nano-precipitates in a half-Heusler matrix after crystallization at 893 K. Moreover, we measured an enhanced Seebeck coefficient for this specimen, which could be ascribed to a reduced carrier concentration as compared to the specimen crystallized at 783 K. Such a reduced carrier concentration could be related to the filtering of low energy electrons at the coherent phase boundaries between full-Heusler precipitates and the half-Heusler matrix as well as to the formation of mid-gap states and a reduction of the energy bandgap by Co interstitials in the half-Heusler phase. We envision that the proposed approach for obtaining a nanostructured thermoelectric material from crystallization of an amorphous precursor can be extended to other material systems for thermoelectric and other functional applications.

4. Material and methods

4.1. Specimen preparation

An alloy ingot of $NbCo_{1.1}Sn$ composition was prepared by vacuum arc melting under a high-purity Ar (> 99.999%) atmosphere using high purity elements (Nb,Co > 99.95%, Sn > 99.99%). Amorphous ribbons were prepared from the ingot by means of melt-spinning. The master alloy was re-melted in a quartz tube by electromagnetic induction and ejected through a nozzle onto a Cu wheel, rotating at a speed of 40 m s^{-1}. The amorphous as-spun ribbons were annealed at 783 and 893 K for 2 h in a tube furnace under a high-purity Ar (> 99.999%) atmosphere. In order to prevent oxidation, the ribbons were wrapped into a Ta sheet.

Reference bulk specimens of NbCoSn half-Heusler and $NbCo_2Sn$ full-Heusler compositions were fabricated for measurements of electrical properties. Alloy ingots were prepared by vacuum arc melting and used for melt-spinning under identical conditions as described above. In contrast to the $NbCo_{1.1}Sn$ alloy, flakes were obtained instead of ribbons, which were crushed into fine powders by ball milling. Ball milling was performed using a planetary ball mill (Nano Ceratech NCTP-05 L) at a ball to powder ratio of 15:1. The resulting powders were sintered in a spark-plasma sintering machine at a temperature of 953 K and a load of 50 MPa for 5 min in vacuum.

4.2. Microstructural characterization

Chemical compositions of as-spun ribbons were measured using ICP-OES (Thermo Fisher Scientific ICAP 6500). XRD (RIGAKU SmartLab operated at 45 kV and 200 mA) measurements were done using Cu Kα radiation (λ = 1.5406 Å). Microstructural characterization was performed by means of STEM (FEI Titan cubed G2 60–300 operated at

300 kV) in combination with EDX analyses and HAADF imaging. APT analyses were performed using a local electrode atom probe (CAMECA LEAP 4000X HR) in pulsed laser mode at a specimen base temperature of ~ 40 K. The laser pulse energy and frequency were set to 50 pJ and 125 kHz, respectively. Data reconstruction and analyses were done with the IVAS 3.8.2 software, provided by CAMECA Instruments. The overlapping peaks of Co^{+} and Sn^{2+} ions at the mass-to-charge ratio of 59 Da was assigned to Sn, as the main isotopic peak of Sn occurs at this value, which resulted in an underestimation of the Co concentration and an overestimation of the Sn concentration by about 0.4 at%. A dual-beam focused ion beam (FIB) - scanning electron microscopy (SEM) system (FEI Helios NanoLab 450 F1) was used to fabricate TEM and APT specimens for correlative analyses similar to the protocols described in [56,57].

4.3. Measurements of thermoelectric properties

Annealed ribbons of (~ 20 × 1 × 0.02 mm^3) were attached at both ends to a Si/SiO_2 (thickness of SiO_2: 500 nm) substrate (2 × 2 cm^2 in area) using silver paste. Seebeck coefficients were measured from room temperature to 873 K in a N_2 atmosphere using the four-probe method [58]. Carrier concentration, Hall mobility, and electrical conductivity were measured at 310, 410, 510, 610, and 710 K (maximum measurement temperature) using a Hall measurement system (ECOPIA HMS-5300/AMP55T3). Three specimens were analyzed to determine average values. UPS (Kratos Axis-Supra) was performed at a photon energy of 21.2 eV (He I) on the NbCoSn and $NbCo_2Sn$ bulk specimens in order to measure their work functions. Prior to these measurements, the sample surfaces were cleaned for 120 s using Ar cluster sputtering at 10 keV. Rectangular shaped NbCoSn and $NbCo_2Sn$ bulk specimens (2 × 2 × 10 mm^3) were used to measure the electrical conductivity with a commercial equipment (BluSys BS1) using the standard four-probe method. The measurements were performed from room temperature to 973 K under a He atmosphere. We measured the thermal conductivities of the as-spun $NbCo_{1.1}Sn$, NCS-783, and NCS-893 specimens at room temperature using the time-domain thermoreflectance (TDTR) method (Transometer^{n8} thermoreflectance metrology system, Richardson, USA). Measurements were done ten times on three specimens for each state. Specimens were polished to 1 μm finish and an Au film of 300 nm in thickness was deposited on the specimen surface to enhance absorption of the incident beam (wave length regime of visible light).

4.4. First-principles calculations

First-principles DFT calculations [59,60] were performed using the Vienna ab initio simulation package (VASP) [61]. The total energies and forces were calculated using the projector augmented wave method [62] together with the generalized gradient approximation for the exchange-correlation potential parametrized by Perdew, Burke and Ernzerhof [63]. The single-electron wavefunctions were expanded using plane waves up to an energy cutoff of 500 eV. An energy tolerance of 10^{-7} was used as a convergence criterion for the self-consistent electronic loop. All lattice parameters and atomic positions were relaxed until the residual forces acting on each atom were below 0.0001 eV $Å^{-1}$. Such a strict choice of cut-off parameters and convergence criteria resulted in DFT energies with an error ≤ 0.1 meV $atom^{-1}$.

For the calculation of work functions, a slab model was built with the unit cell duplicated in the *z* direction while obeying periodic boundary conditions along *x* and *y* directions. The convergence of the work function with respect to the number of atomic layers in the slab supercell was systematically studied for both half-Heusler (i.e. NbCoSn) and full-Heusler (i.e. $NbCo_2Sn$) systems. Based on this analysis, a slab supercell of 1 × 1 × 8 size was chosen, which comprised 48 atoms and 16 at. layers for NbCoSn and 64 atoms and 16 at. layers for $NbCo_2Sn$ (Fig. S11). Vacuum slabs of approximately 23.9 Å and 24.7 Å in thickness were inserted between adjacent slabs in the *z* direction for NbCoSn and $NbCo_2Sn$, respectively. All atomic positions in the slab supercell were further relaxed until the force on each atom was less than 0.01 eV $Å^{-1}$. For the Brillouin zone sampling, the tetrahedron method [64] with a *k*-point grid of 16 × 16 × 2 was employed for both systems.

The defect formation energies were calculated for 2 × 2 × 2 supercells comprising 96 atoms. For the Co interstitials in the half-Heusler, 96 + n atoms were used where the number of Co interstitials, n, were chosen to be 0, 1 and 2. A Γ centered *k*-point grid of 6 × 6 × 6 was used to obtain relaxed lattice parameters and atomic positions. For the case of n = 2, the energetics of all possible configurations were systematically investigated. The lowest energy configuration thus obtained was chosen for comparison with the corresponding results for n = 0 and 1. For the calculations of density of states (DOS), a dense *k*-point grid of 14 × 14 × 14 was employed for NbCoSn with Co interstitials.

CRediT authorship contribution statement

Pyuck-Pa Choi and Seong-Hoon Yi developed the research concept and supervised the research. Chanwon Jung prepared the materials and performed the experiments. Biswanath Dutta and Poulumi Dey performed the theoretical calculations. Seong-jae Jeon and Seungwoo Han contributed to the measurements of the Seebeck coefficient and electrical conductivity. Hyun-Mo Lee and Jin-Seong Park contributed to the Hall measurements. All authors contributed to the scientific discussions and writing of the manuscript.

Declaration of Competing Interest

The authors declare that they have no known competing financial interests or personal relationships that could have appeared to influence the work reported in this paper.

Acknowledgement

This work was supported by the National Research Foundation of Korea (NRF) (grant number 2018R1A4A1022260).

Supplementary data

Additional information about DSC and XRD analyses of as-spun and annealed $NbCo_{1.1}Sn$ specimens are provided together with STEM, HR-TEM, EDX, and APT data of annealed specimens. Temperature dependent electrical conductivities, power factors, and Hall measurement results of the NCS-783 and NCS-893 specimen are presented as well. Finally, the formation energies of the point defects and a supercell of the $NbCo_2Sn$ compound for DFT calculations are provided.

Appendix A. Supporting information

Supplementary data associated with this article can be found in the online version at doi:10.1016/j.nanoen.2020.105518.

References

[1] G.J. Snyder, E.S. Toberer, Complex thermoelectric materials, Nat. Mater. 7 (2008) 105–114, https://doi.org/10.1038/nmat2090.
[2] G. Chen, M.S. Dresselhaus, G. Dresselhaus, J.P. Fleurial, T. Caillat, Recent developments in thermoelectric materials, Int. Mater. Rev. 48 (2003) 45–66, https://doi.org/10.1179/095066003225010182.
[3] A.J. Minnich, M.S. Dresselhaus, Z.F. Ren, G. Chen, Bulk nanostructured thermoelectric materials: current research and future prospects, Energy Environ. Sci. 2 (2009) 466–479, https://doi.org/10.1039/b822664b.
[4] S. Chen, Z. Ren, Recent progress of half-Heusler for moderate temperature thermoelectric applications, Mater. Today 16 (2013) 387–395, https://doi.org/10.1016/j.mattod.2013.09.015.
[5] T. Varghese, C. Dun, N. Kempf, M. Saeidi-Javash, C. Karthik, J. Richardson, C. Hollar, D. Estrada, Y. Zhang, Flexible thermoelectric devices of ultrahigh power factor by scalable printing and interface engineering, Adv. Funct. Mater. 30 (2020) 1–8, https://doi.org/10.1002/adfm.201905796.

[6] Y. Wang, L. Yang, X.L. Shi, X. Shi, L. Chen, M.S. Dargusch, J. Zou, Z.G. Chen, Flexible thermoelectric materials and generators: challenges and innovations, Adv. Mater. 31 (2019) 1–47, https://doi.org/10.1002/adma.201807916.

[7] B. Hinterleitner, I. Knapp, M. Poneder, Y. Shi, H. Müller, G. Eguchi, C. Eisenmenger-Sittner, M. Stöger-Pollach, Y. Kakefuda, N. Kawamoto, Q. Guo, T. Baba, T. Mori, S. Ullah, X.Q. Chen, E. Bauer, Thermoelectric performance of a metastable thin-film Heusler alloy, Nature 576 (2019) 85–90, https://doi.org/10.1038/s41586-019-1751-9.

[8] Lawrence Livemore National Laboratory, Estimated U. S. energy consumption in 2018, ⟨https://flowcharts.llnl.gov/commodities/energy⟩ (accessed: 4, 2020).

[9] C. Forman, I.K. Muritala, R. Pardemann, B. Meyer, Estimating the global waste heat potential, Renew. Sustain. Energy Rev. 57 (2016) 1568–1579, https://doi.org/10.1016/j.rser.2015.12.192.

[10] K. Biswas, J. He, I.D. Blum, C.I. Wu, T.P. Hogan, D.N. Seidman, V.P. Dravid, M. G. Kanatzidis, High-performance bulk thermoelectrics with all-scale hierarchical architectures, Nature 489 (2012) 414–418, https://doi.org/10.1038/nature11439.

[11] J.P. Heremans, V. Jovovic, E.S. Toberer, A. Saramat, K. Kurosaki, A. haroenphakdee, S. Yamanaka, G.J. Snyder, Enhancement of thermoelectric of the electronic density of states, Science 321 (2008) 1457–1461, https://doi.org/10.1126/science.1159725.

[12] B.C. Sales, D. Mandrus, R.K. Williams, Filled skutterudite antimonides: a new class of thermoelectric materials, Science 272 (1996) 1325–1328, https://doi.org/10.1126/science.272.5266.1325.

[13] P.A. Zong, R. Hanus, M. Dylla, Y. Tang, J. Liao, Q. Zhang, G.J. Snyder, L. Chen, Skutterudite with graphene-modified grain-boundary complexion enhances zT enabling high-efficiency thermoelectric device, Energy Environ. Sci. 10 (2017) 183–191, https://doi.org/10.1039/c6ee02467j.

[14] C. Fu, S. Bai, Y. Liu, Y. Tang, L. Chen, X. Zhao, T. Zhu, Realizing high figure of merit in heavy-band p-type half-Heusler thermoelectric materials, Nat. Commun. 6 (2015) 1–7, https://doi.org/10.1038/ncomms9144.

[15] C. Fu, T. Zhu, Y. Liu, H. Xie, X. Zhao, Band engineering of high performance p-type FeNbSb based half-Heusler thermoelectric materials for figure of merit zT > 1, Energy Environ. Sci. 8 (2015) 216–220, https://doi.org/10.1039/c4ee03042g.

[16] H. Zhu, R. He, J. Mao, Q. Zhu, C. Li, J. Sun, W. Ren, Y. Wang, Z. Liu, Z. Tang, A. Sotnikov, Z. Wang, D. Broido, D.J. Singh, G. Chen, K. Nielsch, Z. Ren, Discovery of ZrCoBi based half Heuslers with high thermoelectric conversion efficiency, Nat. Commun. 9 (2018) 1–9, https://doi.org/10.1038/s41467-018-04958-3.

[17] H.J. Lee, K.H. Lee, L. Fu, G.T. Han, H.S. Kim, S. Il Kim, Y.M. Kim, S.W. Kim, Critical role of atomic-scale defect disorders for high-performance nanostructured half-Heusler thermoelectric alloys and their thermal stability, Acta Mater. 180 (2019) 97–104, https://doi.org/10.1016/j.actamat.2019.09.004.

[18] G. Rogl, A. Grytsiv, M. Gürth, A. Tavassoli, C. Ebner, A. Wünschek, S. Puchegger, V. Soprunyuk, W. Schranz, E. Bauer, H. Müller, M. Zehetbauer, P. Rogl, Mechanical properties of half-Heusler alloys, Acta Mater. 107 (2016) 178–195, https://doi.org/10.1016/j.actamat.2016.01.031.

[19] C. Fu, T. Zhu, Y. Pei, H. Xie, H. Wang, G.J. Snyder, Y. Liu, Y. Liu, X. Zhao, High band degeneracy contributes to high thermoelectric performance in p-Type half-Heusler compounds, Adv. Energy Mater. 4 (2014), 1400600, https://doi.org/10.1002/aenm.201400600.

[20] Y. Liu, C. Fu, K. Xia, J. Yu, X. Zhao, H. Pan, C. Felser, T. Zhu, Lanthanide contraction as a design factor for high-performance half-Heusler thermoelectric materials, Adv. Mater. 30 (2018), 1800881, https://doi.org/10.1002/adma.201800881.

[21] H. Zhu, J. Mao, Y. Li, J. Sun, Y. Wang, Q. Zhu, G. Li, Q. Song, J. Zhou, Y. Fu, Discovery of TaFeSb-based half-Heuslers with high thermoelectric performance, Nat. Commun. 10 (2019) 1–8, https://doi.org/10.1038/s41467-018-08223-5.

[22] A. Bhardwaj, D.K. Misra, Improving the thermoelectric performance of TiNiSn half-Heusler via incorporating submicron lamellae eutectic phase of Ti70.5Fe29.5: a new strategy for enhancing the power factor and reducing the thermal conductivity, J. Mater. Chem. A. 2 (2014) 20980–20989, https://doi.org/10.1039/C4TA04661G.

[23] R. Amatya, R.J. Ram, Trend for thermoelectric materials and their earth abundance, J. Electron. Mater. 41 (2012) 1011–1019, https://doi.org/10.1007/s11664-011-1839-y.

[24] J. Shiomi, K. Esfarjani, G. Chen, Thermal conductivity of half-Heusler compounds from first-principles calculations, Phys. Rev. B 84 (2011), 104302, https://doi.org/10.1103/PhysRevB.84.104302.

[25] S.N.H. Eliassen, A. Katre, G.K.H. Madsen, C. Persson, O.M. Løvvik, K. Berland, Lattice thermal conductivity of TixZryHf1-x-yNiSn half-Heusler alloys calculated from first principles: key role of nature of phonon modes, Phys. Rev. B 95 (2017), 045202, https://doi.org/10.1103/PhysRevB.95.045202.

[26] T.J. Zhu, C.G. Fu, H.H. Xie, Y.T. Liu, B. Feng, J. Xie, X.B. Zhao, Lattice thermal conductivity and spectral phonon scattering in FeVSb-based half-Heusler compounds, EPL 104 (2013) 46003, https://doi.org/10.1209/0295-5075/104/46003.

[27] N.S. Chauhan, S. Bathula, A. Vishwakarma, R. Bhardwaj, K.K. Johari, B. Gahtori, A. Dhar, Enhanced thermoelectric performance in p-type ZrCoSb based half-Heusler alloys employing nanostructuring and compositional modulation, J. Mater. 5 (2019) 94–102, https://doi.org/10.1016/j.jmat.2018.11.003.

[28] X. Yan, G. Joshi, W. Liu, Y. Lan, H. Wang, S. Lee, J.W. Simonson, S.J. Poon, T. M. Tritt, G. Chen, Z.F. Ren, Enhanced thermoelectric figure of merit of p-type half-heuslers, Nano Lett. 11 (2011) 556–560, https://doi.org/10.1021/nl104138t.

[29] J.P.A. Makongo, D.K. Misra, X. Zhou, A. Pant, M.R. Shabetai, X. Su, C. Uher, K. L. Stokes, P.F.P. Poudeu, Simultaneous large enhancements in thermopower and electrical conductivity of bulk nanostructured half-Heusler alloys, J. Am. Chem. Soc. 133 (2011) 18843–18852, https://doi.org/10.1021/ja206491j.

[30] Y. Liu, P. Sahoo, J.P.A. Makongo, X. Zhou, S.J. Kim, H. Chi, C. Uher, X. Pan, P.F. P. Poudeu, Large enhancements of thermopower and carrier mobility in quantum dot engineered bulk semiconductors, J. Am. Chem. Soc. 135 (2013) 7486–7495, https://doi.org/10.1021/ja311059m.

[31] M. Gürth, G. Rogl, V.V. Romaka, A. Grytsiv, E. Bauer, P. Rogl, Thermoelectric high ZT half-Heusler alloys Ti1-x-yZrxHfyNiSn ($0 \leq x \leq 1$; $0 \leq y \leq 1$), Acta Mater. 104 (2016) 210–222, https://doi.org/10.1016/j.actamat.2015.11.022.

[32] M. Schrade, K. Berland, S.N.H. Eliassen, M.N. Guzik, C. Echevarria-Bonet, M. H. Sørby, P. Jenuš, B.C. Hauback, R. Tofan, A.E. Gunnæs, C. Persson, O.M. Løvvik, T.G. Finstad, The role of grain boundary scattering in reducing the thermal conductivity of polycrystalline XNiSn (X = Hf, Zr, Ti) half-Heusler alloys, Sci. Rep. 7 (2017) 1–10, https://doi.org/10.1038/s41598-017-14013-8.

[33] M.N. Guzik, C. Echevarria-Bonet, M.D. Riktor, P.A. Carvalho, A.E. Gunnæs, M. H. Sørby, B.C. Hauback, Half-Heusler phase formation and Ni atom distribution in M-Ni-Sn (M = Hf, Ti, Zr) systems, Acta Mater. 148 (2018) 216–224, https://doi.org/10.1016/j.actamat.2018.01.019.

[34] A. Tavassoli, F. Failamani, A. Grytsiv, G. Rogl, P. Heinrich, H. Müller, E. Bauer, M. Zehetbauer, P. Rogl, On the Half-Heusler compounds Nb1-x{Ti,Zr,Hf}xFeSb: phase relations, thermoelectric properties at low and high temperature, and mechanical properties, Acta Mater. 135 (2017) 263–276, https://doi.org/10.1016/j.actamat.2017.06.011.

[35] G. Rogl, P. Sauerschnig, Z. Rykavets, V.V. Romaka, P. Heinrich, B. Hinterleitner, A. Grytsiv, E. Bauer, P. Rogl, V,Nb)-doped half Heusler alloys based on {Ti,Zr,Hf}NiSn with high ZT, Acta Mater. 131 (2017) 336–348, https://doi.org/10.1016/j.actamat.2017.03.071.

[36] T. Kulik, Nanocrystallization of metallic glasses, J. Non Cryst. Solids 287 (2001) 145–161, https://doi.org/10.1016/S0022-3093(01)00627-5.

[37] H.H. Xie, J.L. Mi, L.P. Hu, N. Lock, M. Chirstensen, C.G. Fu, B.B. Iversen, X.B. Zhao, T.J. Zhu, Interrelation between atomic switching disorder and thermoelectric properties of ZrNiSn half-Heusler compounds, CrystEngComm 14 (2012) 4467–4471, https://doi.org/10.1039/C2CE25119A.

[38] C. Fu, M. Yao, X. Chen, L.Z. Maulana, X. Li, J. Yang, K. Imasato, F. Zhu, G. Li, G. Auffermann, Revealing the intrinsic electronic structure of 3D half-heusler thermoelectric materials by angle-resolved photoemission spectroscopy, Adv. Sci. 7 (2020), 1902409, https://doi.org/10.1002/advs.201902409.

[39] Y. Ono, S. Inayama, H. Adachi, T. Kajitani, Thermoelectric properties of doped half-Heuslers NbCoSn1-xSbx and Nb0.99Ti0.01CoSn1-xSbx, Jpn. J. Appl. Physics 45 (2006) 8740–8743, https://doi.org/10.1143/JJAP.45.8740.

[40] Y. Kimura, Y. Tamura, T. Kita, Thermoelectric properties of directionally solidified half-Heusler compound NbCoSn alloys, Appl. Phys. Lett. 92 (2008) 2–5, https://doi.org/10.1063/1.2828713.

[41] M.L.C. Buffon, G. Laurita, N. Verma, L. Lamontagne, L. Ghadbeigi, D.L. Lloyd, T. D. Sparks, T.M. Pollock, R. Seshadri, Enhancement of thermoelectric properties in the Nb-Co-Sn half-Heusler/Heusler system through spontaneous inclusion of a coherent second phase, J. Appl. Phys. 120 (2016), 075104, https://doi.org/10.1063/1.4961215.

[42] R. He, L. Huang, Y. Wang, G. Samsonidze, B. Kozinsky, Q. Zhang, Z. Ren, Enhanced thermoelectric properties of n-type NbCoSn half-Heusler by improving phase purity, APL Mater. 4 (2016), 104804, https://doi.org/10.1063/1.4952994.

[43] D.A. Ferluccio, R.I. Smith, J. Buckman, J.-W.G. Bos, Impact of Nb vacancies and p-type doping of the NbCoSn–NbCoSb half-Heusler thermoelectrics, Phys. Chem. Chem. Phys. 20 (2018) 3979–3987, https://doi.org/10.1039/C7CP07521A.

[44] F. Serrano-Sánchez, T. Luo, J. Yu, W. Xie, C. Le, G. Auffermann, A. Weidenkaff, T. Zhu, X. Zhao, J.A. Alonso, Thermoelectric properties of n-type half-Heusler NbCoSn with heavy-element Pt substitution, J. Mater. Chem. A 8 (2020) 14822–14828, https://doi.org/10.1039/D0TA04644B.

[45] L. Chkoda, C. Heske, M. Sokolowski, E. Umbach, F. Steuber, J. Staudigel, M. Stößel, J. Simmerer, Work function of ITO substrates and band-offsets at the TPD/ITO interface determined by photoelectron spectroscopy, Synth. Met. 111 (2000) 315–319, https://doi.org/10.1016/S0379-6779(99)00355-0.

[46] J.M.D. Coey, M. Venkatesan, Half-metallic ferromagnetism: example of CrO2, J. Appl. Phys. 91 (2002) 8345–8350, https://doi.org/10.1063/1.1447879.

[47] E.H. Rhoderick, Metal-semiconductor contacts, IEE Proc. 129 (1982), https://doi.org/10.1049/ip-i-1.1982.0001.

[48] D.M. Wood, Classical size dependence of the work function of small metallic spheres, Phys. Rev. Lett. 46 (1981) 749, https://doi.org/10.1103/PhysRevLett.46.749.

[49] S.V. Faleev, F. Léonard, Theory of enhancement of thermoelectric properties of materials with nanoinclusions, Phys. Rev. B 77 (2008), 214304, https://doi.org/10.1103/PhysRevB.77.214304.

[50] M. He, J. Ge, Z. Lin, X. Feng, X. Wang, H. Lu, Y. Yang, F. Qiu, Thermopower enhancement in conducting polymer nanocomposites via carrier energy scattering

at the organic-inorganic semiconductor interface, Energy Environ. Sci. 5 (2012) 8351–8358, https://doi.org/10.1039/c2ee21803h.
[51] C. Gayner, Y. Amouyal, Energy filtering of charge carriers: current trends, challenges, and prospects for thermoelectric materials, Adv. Funct. Mater. 1901789 (2019) 1–17, https://doi.org/10.1002/adfm.201901789.
[52] J.E. Douglas, P.A. Chater, C.M. Brown, T.M. Pollock, R. Seshadri, Nanoscale structural heterogeneity in Ni-rich half-Heusler TiNiSn, J. Appl. Phys. 116 (2014), 163514, https://doi.org/10.1063/1.4900497.
[53] C. Colinet, P. Jund, J.C. Tédenac, NiTiSn a material of technological interest: ab initio calculations of phase stability and defects, Intermetallics 46 (2014) 103–110, https://doi.org/10.1016/j.intermet.2013.10.016.
[54] W.G. Zeier, J. Schmitt, G. Hautier, U. Aydemir, Z.M. Gibbs, C. Felser, G.J. Snyder, Engineering half-Heusler thermoelectric materials using Zintl chemistry, Nat. Rev. Mater. 1 (2016) 1–10, https://doi.org/10.1038/natrevmats.2016.32.
[55] S.A. Barczak, J. Buckman, R.I. Smith, A.R. Baker, E. Don, I. Forbes, J.G. Bos, Impact of interstitial Ni on the thermoelectric properties of the half-Heusler TiNiSn, Materials 11 (2018) 536, https://doi.org/10.3390/ma11040536.
[56] J. Mayer, L.A. Giannuzzi, T. Kamino, J. Michael, TEM sample preparation and FIB induced damage, MRS Bull. 32 (2007) 400–407, https://doi.org/10.1557/mrs2007.63.
[57] M. Herbig, P. Choi, D. Raabe, Combining structural and chemical information at the nanometer scale by correlative transmission electron microscopy and atom probe tomography, Ultramicroscopy 153 (2015) 32–39, https://doi.org/10.1016/j.ultramic.2015.02.003.
[58] A. Ahmed, S. Han, Preparation and thermoelectric properties of RF co-sputtered CoSb3 skutteruddite thin films, J. Korean Phys. Soc. 65 (2014) 1614–1618, https://doi.org/10.3938/jkps.65.1614.
[59] P. Hohenberg, W. Kohn, Inhomogeneous electron gas, Phys. Rev. 136 (1964) B864–B871, https://doi.org/10.1103/PhysRev.136.B864.
[60] W. Kohn, L.J. Sham, Self-consistent equations including exchange and correlation effects, Phys. Rev. 140 (1965) A1133–A1138, https://doi.org/10.1103/PhysRev.140.A1133.
[61] G. Kresse, J. Hafner, Ab initio molecular dynamics for open-shell transition metals, Phys. Rev. B. 48 (1993) 13115–13118, https://doi.org/10.1103/PhysRevB.48.13115.
[62] P.E. Blöchl, Projector augmented-wave method, Phys. Rev. B 50 (1994) 17953–17979, https://doi.org/10.1103/PhysRevB.50.17953.
[63] J.P. Perdew, K. Burke, M. Ernzerhof, Generalized gradient approximation made simple, Phys. Rev. Lett. 77 (1996) 3865–3868, https://doi.org/10.1103/PhysRevLett.77.3865.
[64] P.E. Blöchl, O. Jepsen, O.K. Andersen, Improved tetrahedron method for Brillouin-zone integrations, Phys. Rev. B 49 (1994) 16223–16233, https://doi.org/10.1103/PhysRevB.49.16223.

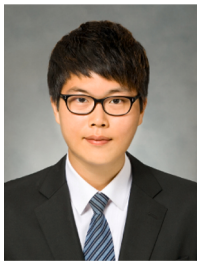

Chanwon Jung received a B.S degree in the division of Materials Science & Engineering from the University of Hanyang in 2015 and M.S degree from Korea Advanced Institute of Science and Technology (KAIST) in 2017. He is currently a Ph.D. student in KAIST under the supervision of Prof. Pyuck-Pa Choi. He studies functional nanostructured materials using advanced characterization techniques, in particular atom probe tomography. His main research interest is to study the linkage between the structure and functional properties especially with a focus on thermoelectrics and electro-catalysis.

Biswanath Dutta is currently a post-doctoral researcher in the Department of Materials Science and Engineering at Delft University of Technology. He obtained his Masters of Science degree in Physics from Gauhati University (India) in 2006. He then received his PhD degree in the field of theoretical Condensed Matter Physics from Indian Institute of Technology Guwahati (India) in 2012. Following this, he joined Max-Planck-Institut für Eisenforschung GmbH (Germany) as post-doctoral scientist. His research interests are focused on ab-initio modelling of thermomagnetic and thermoelectric materials for waste heat recovery and finite temperature excitations in multi-component alloys, e.g., high entropy alloys.

Poulumi Dey is currently an Assistant Professor in the Department of Materials Science and Engineering at Delft University of Technology. She completed her Masters of Science degree in Physics from Indian Institute of Technology Guwahati (IITG) in 2005. She obtained her PhD degree in the field of theoretical Condensed Matter Physics from IITG in 2011. In 2012, she joined Max-Planck-Institut für Eisenforschung GmbH as post-doctoral scientist. Her research interests include ab-initio based designing of technologically relevant materials for better resistance to hydrogen embrittlement and first principles based understanding of precipitation behavior in complex multi-component alloys.

Seong-jae Jeon is a senior researcher at Korea Institute and Machinery and Materials at the department of Nano-Mechatronics. He received his Ph.D. degree in Advanced Materials Science and Engineering from the Sungkyunkwan University Republic of Korea. His research interests are mainly focused on thin film and bulk thermoelectric materials, devices, modules, and their systems for Energy harvesting and cooling.

Seungwoo Han is a principal researcher at Korea Institute and Machinery and Materials and a professor at department of Nano-Mechatronics, University of Science and Technology. He received a Ph.D. degree in Mechanical Engineering from Pusan National University (2006). His research interests include thermoelectric thin films, a micro thermoelectric device, flexible thermoelectric device, and their applications for power generation and hot spot cooling.

Hyun-Mo Lee received a B.S course in the division of Materials Science & Engineering from Hanyang University, Seoul, Korea in 2015. He is currently a Unified M.S and Ph.D. course student in the division of Materials Science & Engineering from Hanyang University, Seoul, Korea. He is studying electrical and photonic devices under the supervisor of Dr. Jin-Seong Park. His main research interests include high mobility thin-film transistors (TFTs) with sputtering and atomic layer deposition (ALD) and thin-film based photosensor for visible to near-infrared region application.

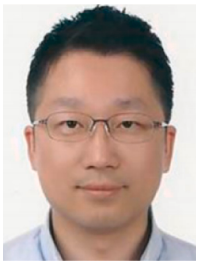

Jin-Seong Park is a professor at the Division of Materials Science & Engineering of Hanyang University, Seoul, Korea. His main research interests include the development of functional thin-film transistors and devices for flexible/transparent/wearable electronics. Before he joined the faculty of Hanyang University in 2013, he was a faculty member at the Department of Materials Science & Engineering of Dankook University, South Korea (2009–2013). He was also a senior researcher at Samsung SDI (2005–2008) and Samsung Mobile Display (2008–2009) as well as a post-doc fellow in the Department of Chemistry, Harvard University from 2003 to 2005.

Seong-Hoon Yi received a B.S and M.S degree from the Korea University in 1986. He obtained his Ph.D. degree in 1997 from the department of materials science and metallurgical engineering at the University of Wisconsin-Madison. He is a professor of materials science and metallurgical engineering at Kyungpook National University, Daegu, Korea. His main research interests include the structural and functional applications of metallic glasses and intermetallic alloys.

Pyuck-Pa Choi received a B.S, M.S., and Ph.D. degree from University of Göttingen in 2003. After working as a postdoctoral researcher at the University of Ulsan, he joined the Korea Institute of Science and Technology as a senior research scientist. Afterwards he worked as the head of research group Atom Probe Tomography at Max-Planck-Institut für Eisenforschung. Since 2016 he is an Associate Professor at the Department of Materials Science and Engineering at Korea Advanced Institute of Science and Technology. His research interests are focused on understanding the structure-composition-property relationships of nanomaterials using advanced characterization techniques, in particular Atom Probe Tomography.